

## Ultrahigh Gain Gyrotron Traveling Wave Amplifier

K. R. Chu, H. Y. Chen, C. L. Hung, T. H. Chang, and L. R. Barnett

*Department of Physics, National Tsing Hua University, Hsinchu, Taiwan, Republic of China*

S. H. Chen

*National Center for High-Performance Computing, Hsinchu, Taiwan, Republic of China*

T. T. Yang

*Synchrotron Radiation Research Center, Hsinchu, Taiwan, Republic of China*

(Received 29 July 1998)

Mode competition in the gyrotron traveling wave amplifier is shown to be intricately connected to the interplay between the absolute/convective instabilities, circuit losses, and reflective feedback. Physical origins of spurious oscillations are analyzed and characterized. Fundamental understanding of these processes leads to a device concept which provides zero-drive stability at ultrahigh gain. The scheme was verified in a proof-of-principle experiment in the  $Ka$  band, producing 93 kW saturated peak power at 26.5% efficiency, 70 dB gain, and a 3 dB bandwidth of 3 GHz. [S0031-9007(98)07703-5]

PACS numbers: 84.40.Ik, 84.40.Fe

The millimeter-wave region of the electromagnetic spectrum is a relatively unexploited band between the microwave and optical frequencies. A myriad of applications [1] of millimeter waves are being conceived which require powerful sources well beyond currently available technology. The electron cyclotron maser mechanism discovered in the 1950s has since evolved from a basic relativistic physics effect into a new class of millimeter wave devices referred to as the gyrotron. Consider an electron beam in which electrons move in helical orbits in an external magnetic field. Because of the relativistic mass dependence of the cyclotron frequency, the electrons in the rf field will bunch in their gyrational phase space and thereby amplify the rf field which causes the bunching to occur. The gyrotron traveling wave amplifier (gyro-TWA) is an amplifier version of the gyrotron which features a fast-wave structure for high-power and broad-band interaction [2–6]. The current paper reports studies of the key physics issues of the gyro-TWA as well as the experimental demonstration of the gyro-TWA as a millimeter-wave amplifier of unprecedented capabilities in power, gain, bandwidth, and efficiency.

In contrast to conventional linear beam microwave devices such as the traveling wave tube (TWT), the electron beam employed in the gyrotron possesses a transverse motion at the electron cyclotron frequency. It is this property that allows the beam to selectively interact with a high order waveguide mode at a high cyclotron harmonic by properly matching the resonance conditions. However, the additional degree of freedom provided by the multitude of cyclotron harmonics can also generate numerous spurious oscillations. Interactions with backward waves are sources of absolute instabilities [7–12], whereas the forward wave interactions are normally, but not always, convective instabilities [12]. The various absolute instabilities can easily be the dominant sources of oscillations in the gyro-TWA.

Feedback due to reflections at structural nonuniformities presents a different source of oscillation in the high gain regime (referred to as the reflective oscillation). Reflective oscillations can be effectively eliminated by a sever as has been a standard practice in TWT's. However, the absolute instability is basically different from the reflective oscillation in that the backward wave associated with the absolute instability is internally generated by the ac electron beam current. With the beam providing an internal path, the sever cannot really quite separate the interaction structure into two isolated sections to produce a substantial stabilizing effect. Recently, an interaction structure (Fig. 1) with distributed wall losses was shown to be effective in suppressing both types of oscillations [13]. In Fig. 1, the lossy section ( $L_1$ ) and conducting-wall section ( $L_2$ ) comprise the linear and nonlinear stages of the amplification, respectively. Like the sever, the lossy section cuts off the path of the reflective feedback loop. In contrast to the sever, however, it forms the linear amplification stage. To the predominantly backward power flow of the absolute instability, the lossy section also functions as an effective energy sink.

We shall show that the distributed-loss structure can also yield ultrahigh stable gain. The scheme is based on the different responses to wall losses between the cold tube and

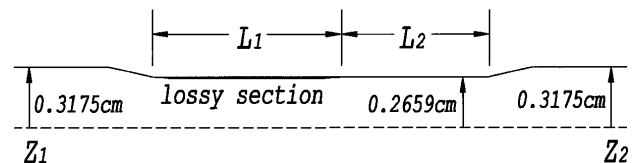


FIG. 1. Schematic of a  $Ka$  band,  $TE_{11}$  mode, fundamental harmonic gyro-TWA. Lossy section  $L_1$  and conducting-wall section  $L_2$  form the interaction region. The ends are tapered for broadband coupling.

hot tube modes. The cold tube mode has all of its energy in the electromagnetic fields. In a hot tube, however, the energy of the beam generated mode resides not only in the electromagnetic fields but also in the oscillatory motion of the electrons, the latter being an integral part of the hot tube mode. The lossy wall absorbs the electromagnetic energy, but not the oscillatory kinetic energy of the electrons. Thus, wall losses attenuate the reflected wave (basically a cold tube mode) significantly more than they reduce the gain of the amplifying wave (a hot tube mode). It can be shown analytically [14] that the reduction in hot tube gain due to wall losses is only one third of the cold tube attenuation over the same distance. Such unequal effects can be exploited to simultaneously achieve both high gain and stability in a scheme in which the linear section ( $L_1$ ) is made sufficiently long to provide the desired gain, while the nonlinear section ( $L_2$ ) is constrained to a minimum length to enhance the threshold of absolute instabilities.

We first analyze three types of oscillations based on the configuration of Fig. 1 by employing the trajectory tracing technique [15–17] to follow the beam and wave dynamics throughout the entire structure. Imposition of physical boundary conditions at both ends allows the evaluation of a self-consistent rf field profile  $f(z)$  to account for wave reflections at all interfaces and nonuniformities. Such details in the modeling allow oscillations of various origins to be studied on the basis of the overall rather than sectionalized interaction structure. Properties of oscillations are illustrated below for the structural dimensions of

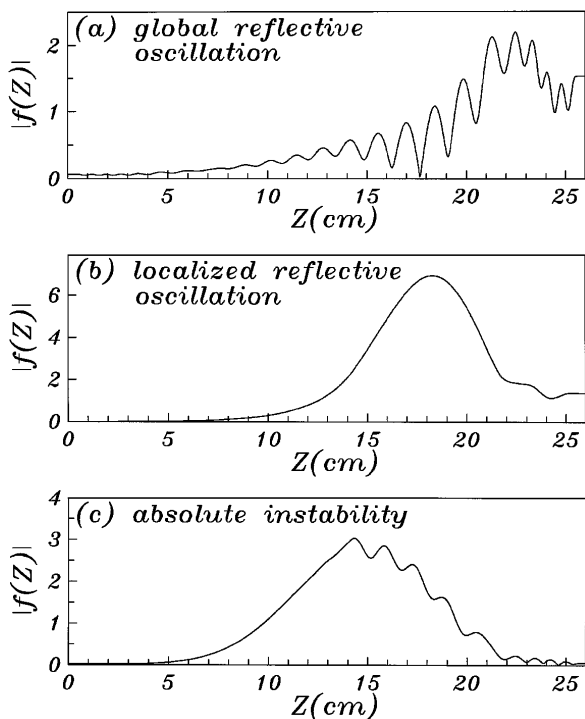


FIG. 2. Calculated profiles of the rf field amplitude  $|f(z)|$  in the structure of Fig. 1 for (a) the global reflective oscillation, (b) the localized reflective oscillation, and (c) the absolute instability.

Ref. [13]. However, the qualitative features are of a general nature.

Reflective oscillations of a global nature start when the total gain exceeds the reflection at the input/output ends plus the attenuation in the lossy section (all in dB). Figure 2(a) shows the field profile of a typical global reflective oscillation. Calculations indicate that the oscillation can be stabilized by lowering the operating current  $I_b$  [Fig. 3(a)] and magnetic field  $B_0$  [Fig. 3(c)], or by increasing the wall resistivity  $\rho$  [Fig. 3(b)].

The conducting-wall section ( $L_2$ ) by itself is subject to localized oscillations due to reflections at the lossy-wall junction on the left and the output structure on the right. Figure 2(b) illustrates the field profile of such an oscillation in the  $TE_{111}$  mode. Since the oscillation is localized to the conducting-wall section, the oscillation power is found to be nearly independent of the length  $L_1$  [Fig. 4(a)] and wall resistivity  $\rho$  [normalized to that of copper  $\rho_{cu} = 1.72 \times 10^{-8} \Omega m$ , Fig. 2(b)] of the lossy section. These two features are in contrast to the high sensitivity of the global reflective oscillation to  $L_1$  and  $\rho$ . Figure 4(c) demonstrates the sensitivity of the oscillation power and frequency versus the operating magnetic field.

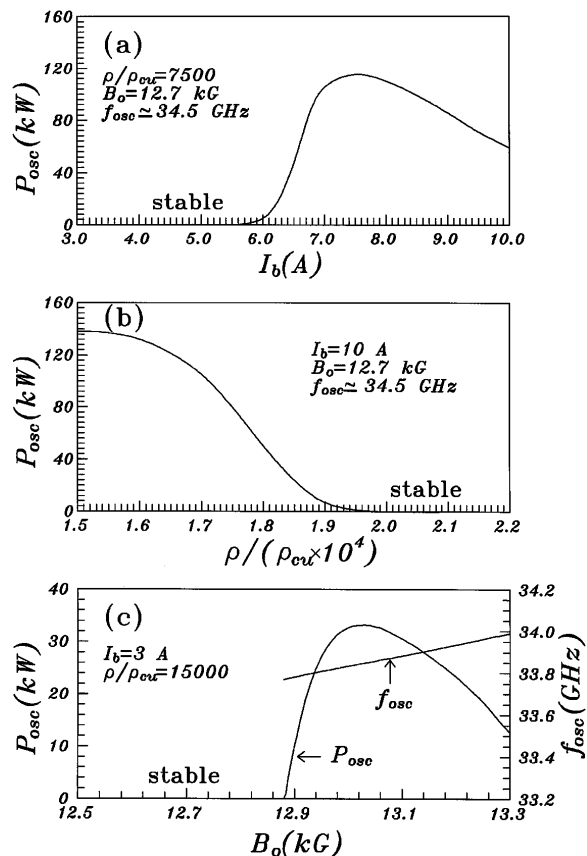


FIG. 3. Calculated power of global reflective oscillations ( $TE_{11}$  mode,  $s = 1$ ) versus (a) beam current  $I_b$ , (b) wall resistivity  $\rho$  of the lossy section, and (c) magnetic field  $B_0$ . Parameters used are (refer to Fig. 1)  $L_1 = 9.73$  cm,  $L_2 = 7.73$  cm,  $V_b = 100$  kV,  $\alpha = 0.85$ ,  $r_c = 0.09$  cm, and  $\Delta v_z/v_z = 0$ , where  $r_c$  is the guiding center position.

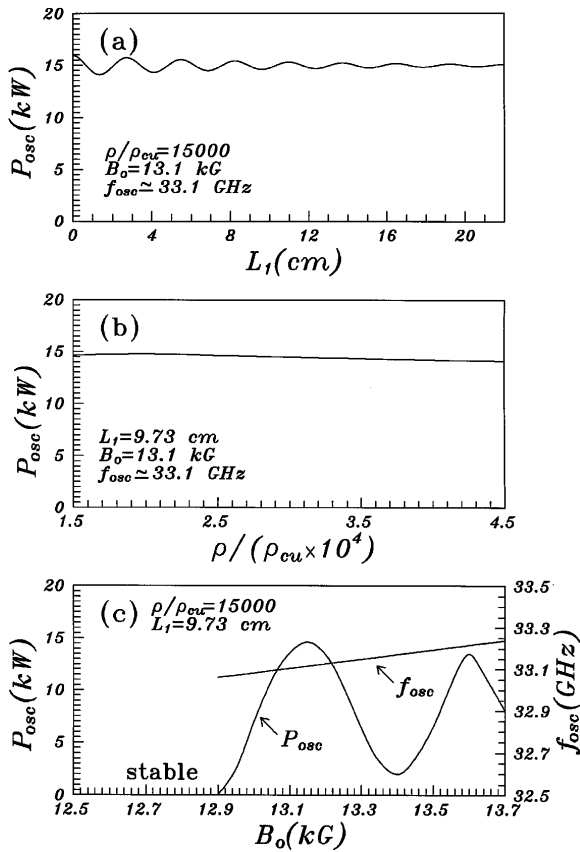


FIG. 4. Calculated power of localized reflective oscillations (TE<sub>111</sub> mode,  $s = 1$ ) in the conducting-wall section versus (a) length  $L_1$  of the lossy section, (b) wall resistivity  $\rho$  of the lossy section, and (c) magnetic field  $B_0$ .  $I_b = 3$  A and other parameters are the same as in Fig. 3 unless denoted otherwise.

The gyro-TWA under study (Fig. 1) is most susceptible to the TE<sub>21</sub> mode absolute instability at the second cyclotron harmonic [10]. Figure 2(c) illustrates the field profile of such an oscillation. Figure 5 displays the start-oscillation current ( $I_{st}$ ) versus the electron pitch angle  $\alpha$  ( $= v_{\perp}/v_z$ ) for different values of  $\rho$ .  $I_{st}$  decreases with increasing  $\alpha$  as expected. Again, the wall resistivity is shown to have a strong stabilizing effect. Increasing the wall resistivity will allow stable operation at higher  $I_b$  and  $\alpha$  values, hence achieve higher power and efficiency.

An experimental gyro-TWA was assembled to verify the ultrahigh gain scheme just described. A mechanically tunable magnetron injection electron gun [18] was attached to the interaction structure of Fig. 1. Lengths of the graphite-coated lossy section ( $L_1 = 20$  cm with  $\sim 100$  dB loss corresponding to  $\rho = 3.6 \times 10^4 \rho_{cu}$ ) and the conducting-wall section ( $L_2 = 4$  cm) were chosen to achieve high gain as well as overall stability. Input/output waves were coupled at  $z_1$  and  $z_2$  through the side walls with oscillation-free couplers which also function as converters between circularly and linearly polarized waves. The magnetic field was provided by a superconducting magnet. Output power at low duty was measured with a calibrated crystal detector (with estimated accuracy of  $\pm 5\%$ ) and

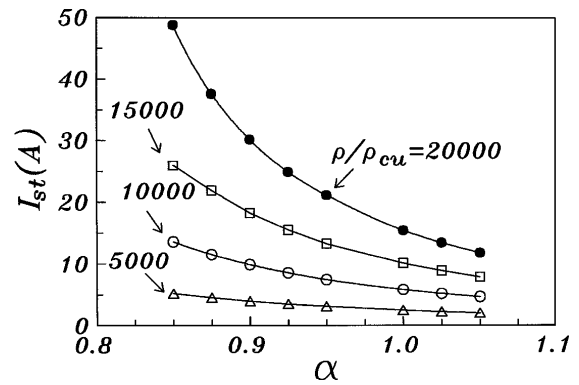


FIG. 5. Calculated start-oscillation current of the second harmonic absolute instability (TE<sub>21</sub> mode,  $f_{osc} \approx 56$  GHz) versus the electron pitch angle  $\alpha$  for different values of wall resistivity  $\rho$ .  $V_b = 100$  kV,  $L_1 = 9.73$  cm,  $L_2 = 7.73$  cm,  $B_0 = 12.5$  kG, and  $r_c = 0.09$  cm.

verified with a calorimeter (agreement was within  $\sim 5\%$ ). At the operating beam current of 3.5 A, the gyro-TWA was found to be zero-drive stable from all three types of instabilities in the optimum range of operating magnetic field ( $12.65 < B_0 < 12.75$  kG). As the magnetic field was increased, a localized reflective oscillation was observed and identified to be the TE<sub>111</sub> mode of the conducting-wall section (Fig. 6). At still higher magnetic field, mode jumping was also observed. Note that in Fig. 6 characteristics of the observed oscillation power and frequency are very similar to the theoretically predicted behavior shown in Fig. 4(c).

Figure 7 plots the saturated output power and gain (dots) as functions of the frequency. The peak power of 93 kW corresponds to a saturated gain of 70 dB and efficiency of 26.5%. The ultrahigh gain, 30 dB beyond that previously achieved, permits the use of solid-state sources as drivers. The full width at half maximum bandwidth is 3 GHz, approximately 8.6% of the center frequency. Measured data are closely matched by theoretical predictions (solid line) using the simulated beam parameters [18]  $\alpha = 1$ ,  $\Delta v_z/v_z = 5\%$ , and  $r_c = 0.09$  cm, where  $\Delta v_z/v_z$  is the electron velocity spread and  $r_c$  is the radial position of

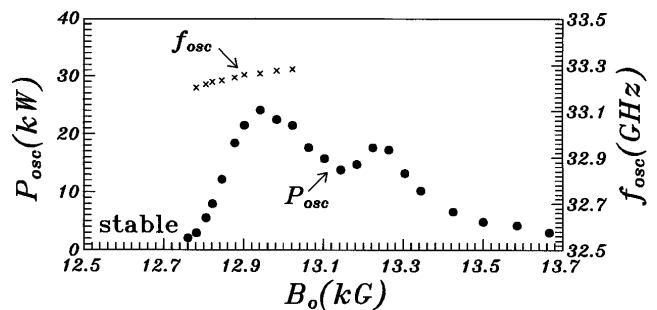


FIG. 6. Measured power (dots) and frequency (crosses) of spurious oscillations at zero-drive power versus the magnetic field. Optimum operating magnetic field of the gyro-TWA (for Figs. 7 and 8) lies in the stable region.

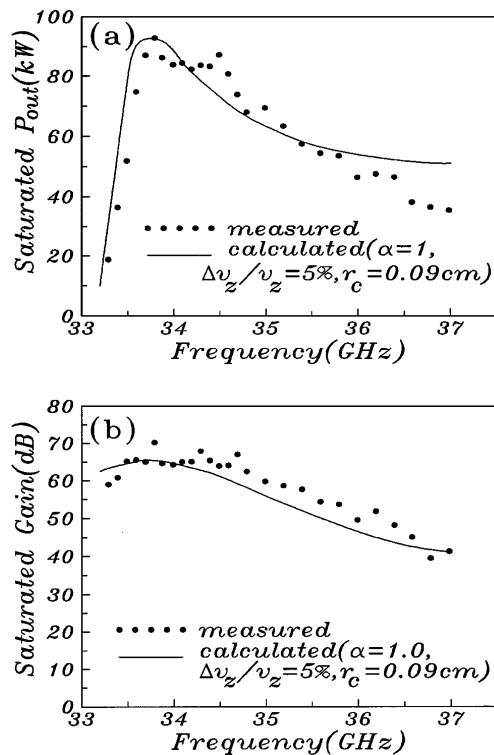


FIG. 7. Saturated output power (a) and gain (b) versus the frequency. Measured and calculated data are shown by dots and lines, respectively.  $V_b = 100$  kV,  $I_b = 3.5$  A, and  $B_0 = 12.7$  kG.

the electron guiding centers. The theory also predicts that the saturated power is almost independent of the length of the lossy section while the gain is linearly proportional to it. The peak Ohmic power dissipated on the lossy walls is calculated to be approximately 10 kW, or  $\sim 300$  W/cm<sup>2</sup>. The average-power handling capability will be limited by the availability of proper heat-resistant lossy materials and advanced cooling techniques. Supplementary attenuation by broadband side-wall coupling to an external load could conceivably be implemented to remove this limitation.

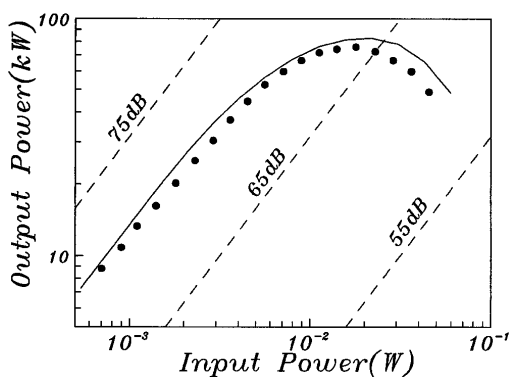


FIG. 8. Measured (dots) and calculated (lines) output power versus the drive power.  $V_b = 100$  kV,  $I_b = 3.5$  A,  $B_0 = 12.7$  kG, and  $f = 34.2$  GHz.

Figure 8 shows the measured output power versus the input power (dots). Linear and saturated behaviors are consistent with the calculated data (solid line). Again,  $\alpha = 1$ ,  $\Delta v_z/v_z = 5\%$ , and  $r_c = 0.09$  cm were assumed in the calculations. In all the measurements for Figs. 7 and 8, we have not detected any spurious oscillation.

These studies indicate that a basic understanding of the intricate interplay between the absolute/convective instabilities, circuit losses, and reflective feedback is of fundamental importance to the scientific demonstration of the potential capability of the gyro-TWA. Significantly higher power can be obtained by employing the harmonic cyclotron maser interaction [6,19].

This work was supported by the National Science Council, ROC. The authors are grateful for many stimulating discussions with Professor Neville C. Luhmann, Jr.

- [1] *Application of High Power Microwaves*, edited by A. V. Gaponov-Grekhov and V.L. Granatstein (Artech House, Boston, MA, 1994).
- [2] J.L. Seftor, V.L. Granatstein, K.R. Chu, P. Sprangle, and M.E. Read, *IEEE J. Quantum Electron.* **15**, 848 (1979).
- [3] L.R. Barnett, K.R. Chu, J.M. Baird, V.L. Granatstein, and A.T. Drobot, in *Technical Digest of the International Electron Devices Meeting* (IEEE, New York, 1979), pp. 164–167.
- [4] R.S. Symons, H.R. Jory, S.J. Hegji, and P.E. Ferguson, *IEEE Trans. Microwave Theory Tech.* **29**, 181 (1981).
- [5] G.S. Park, J.J. Choi, C.K. Chong, A.K. Ganguly, and R.H. Kyser, in *Technical Digest of International Electron Device Meeting* (IEEE, New York, 1993), pp. 351–353.
- [6] Q.S. Wang, D.B. McDermott, and N.C. Luhmann, Jr., *Phys. Rev. Lett.* **75**, 4322 (1995).
- [7] Y.Y. Lau, K.R. Chu, L.R. Barnett, and V.L. Granatstein, *Int. J. Infrared Millim. Waves* **2**, 373 (1981).
- [8] J.A. Davies, *Phys. Fluids B* **1**, 663 (1989).
- [9] A.T. Lin and C.C. Lin, *Phys. Fluids B* **1**, 2286 (1989).
- [10] L.R. Barnett, L.H. Chang, H.Y. Chen, K.R. Chu, Y.K. Lau, and C.C. Tu, *Phys. Rev. Lett.* **63**, 1062 (1989).
- [11] K.R. Chu, L.R. Barnett, W.K. Lau, L.H. Chang, A.T. Lin, and C.C. Lin, *Phys. Fluids B* **3**, 2403 (1991).
- [12] K.R. Chu and A.T. Lin, *IEEE Trans. Plasma Sci.* **16**, 90 (1988).
- [13] K.R. Chu, L.R. Barnett, H.Y. Chen, S.H. Chen, Ch. Wang, Y.S. Yeh, Y.C. Tsai, T.T. Yang, and T.Y. Dawn, *Phys. Rev. Lett.* **74**, 1103 (1995).
- [14] Y.Y. Lau, K.R. Chu, L.R. Barnett, and V.L. Granatstein, *Int. J. Infrared Millim. Waves* **2**, 395 (1981).
- [15] P. Sprangle and W.M. Manheimer, *Phys. Fluids* **18**, 224 (1975).
- [16] A.K. Ganguly and S. Ahn, *Int. J. Electron.* **53**, 641 (1982).
- [17] A.W. Fliflet, *Int. J. Electron.* **61**, 1049 (1986).
- [18] Ch. Wang, Y.S. Yeh, T.T. Yang, H.Y. Chen, S.H. Chen, Y.C. Tsai, L.R. Barnett, and K.R. Chu, *Rev. Sci. Instrum.* **68**, 3031 (1997).
- [19] A.T. Lin, K.R. Chu, C.C. Lin, C.S. Kou, D.B. McDermott, and N.C. Luhmann, Jr., *Int. J. Electron.* **72**, 873 (1992).